

Communication

Switchable Metasurface with VO₂ Thin Film at Visible Light by Changing Temperature

Jin-Kyu Yang ^{1,2,*}  and Hyeon-Seok Jeong ¹

¹ Department of Optical Engineering, Kongju National University, Cheonan 31080, Korea; 201402146@smail.kongju.ac.kr

² Institute of Application and Fusion for Light, Kongju National University, Cheonan 31080, Korea

* Correspondence: jinkyuyang@kongju.ac.kr

Abstract: We numerically demonstrated switchable metasurfaces using a phase change material, VO₂ by temperature change. The Pancharatnam–Berry metasurface was realized by using an array of Au nanorods on top of a thin VO₂ film above an Au film, where the optical property of the VO₂ film is switched from the insulator phase at low temperature to the metal phase at high temperature. At the optimal structure, polarization conversion efficiency of the normal incident light is about 75% at low temperature while that is less than 0.5% at high temperature in the visible region ($\lambda \sim 700$ nm). Various functionalities of switchable metasurfaces were demonstrated such as polarization conversion, beam steering, Fourier hologram, and Fresnel hologram. The thin-VO₂-film-based switchable metasurface can be a good candidate for various switchable metasurface devices, for example, temperature dependent optical sensors, beamforming antennas, and display.

Keywords: metasurface; switchable; phase change materials; VO₂; hologram



Citation: Yang, J.-K.; Jeong H.-S. Switchable Metasurface with VO₂ Thin Film by Changing Temperature. *Photonics* **2021**, *8*, 57. <https://doi.org/10.3390/photronics8020057>

Received: 20 January 2021
Accepted: 16 February 2021
Published: 18 February 2021

Publisher's Note: MDPI stays neutral with regard to jurisdictional claims in published maps and institutional affiliations.



Copyright: © 2021 by the authors. Licensee MDPI, Basel, Switzerland. This article is an open access article distributed under the terms and conditions of the Creative Commons Attribution (CC BY) license (<https://creativecommons.org/licenses/by/4.0/>).

1. Introduction

Metasurfaces have attracted much attention as fascinating optical elements because of flat and ultrathin subwavelength structures that manipulate the phase, amplitude, and polarization of an incident light [1–3]. In contrast to conventional optical elements, metasurfaces provide abrupt phase changes of an incident light, which enable metasurfaces to have a unique functionality to form an arbitrary wavefront of a light beam, for example, beam shaping [1,4–7], polarization control [8–12], ultrathin lens [13–16], and holography [17–21].

There are several methods to realize an additional phase change at the metasurface. First, multi-resonance plasmonic elements were adapted on the metasurface which has the same reflectivity with desired phase changes [1,22,23]. Another method, the Pancharatnam–Berry (PB) phase, has been widely used because of continuous change of phase delay with constant transmittance (or reflectance) by simple geometrical rotation [24–26]. However, in order to get the anomalous refraction behavior, the incident beam should have a circular polarization. All dielectric Huygens' metasurfaces with high-refractive-index dielectric rods are the alternative way to get high transmission without polarization sensitivity by overlapping electric and magnetic resonances at the same wavelength [27–29].

Recently, it has been reported that the optical properties of the metasurface could be actively controlled by using various tuning methods, for example, mechanical stretch, field effect, and phase change behavior [30–33]. Especially, phase change materials (PCMs) such as germanium antimony tellurium alloy (Ge₂Sb₂Te₅, GST) and vanadium dioxide (VO₂) have been intensively investigated due to their switchable ability of optical properties [34–36]. VO₂ is one of the most interesting PCMs because of the unique metal-insulator-transition behavior which could be realized both thermally and electrically [37]. Unlike the GST, the phase transition of the VO₂ from the insulating phase to the metallic phase occurs by temperature around 70 °C which could exist in nature [35,36]. However, most of switchable metasurfaces using VO₂ were realized in the mid-infrared (IR) or THz

region not yet in the visible range [38–40]. One recent paper reported that reconfigurable multistate optical system for dynamic display was demonstrated by phase transition of VO₂ film modulated by temperature, hydrogen-doping, and electron-doping [41]. In this paper, we demonstrated a switchable metasurface with a VO₂ thin film in the visible region ($\lambda = 700$ nm). The reflectarray metasurface was designed based on PB-phase principle, and possible applications of switchable metasurfaces, such as polarization conversion, beam steering, Fourier hologram, and Fresnel hologram were numerically performed. We believe that VO₂ based metasurfaces in the visible region can provide a practical platform for various applications of dynamic switch by temperature.

2. Materials and Methods

2.1. Optical Properties of VO₂

The PCMs have fascinated many researchers due to their optical and electrical capabilities of active control. In this paper, we used the classical dispersion model based on the Drude–Lorentz model to realize the optical constant of a thin VO₂ film in both the insulator and the metal phase for dispersive Finite-Difference Time-Domain (FDTD) method with auxiliary differential equation [42,43]. It is worth noting that low temperature for insulating phase of VO₂ is below 30 °C and high temperature for metallic phase is above 90 °C [35,36,42,44]. The equation to describe the complex permittivity of the VO₂ can be expressed by

$$\epsilon(\omega) = \epsilon_\infty + \sum_{p=1,2} \frac{f_p \omega_p^2}{\omega_p^2 - \omega^2 - i\gamma_p \omega'} \tag{1}$$

where two poles of the Drude–Lorentz model were used to describe the dielectric constant of the VO₂ film at low temperature and at high temperature, summarized in Table 1. Here, there is no Drude oscillator due to the plasma frequency far from the visible or near-IR region and the sufficiently large Drude collision rate [44].

Table 1. The parameters of two poles of the Drude–Lorentz model for the dielectric constant of VO₂ from the visible to the IR region, directly taken from Ref. [44]. Here, the unit of ω_p and γ_p are \hbar^{-1} eV.

VO ₂ (Low T)	$\epsilon_\infty = 3.4$			VO ₂ (High T)	$\epsilon_\infty = 4.5$		
p	f_p	ω_p	γ_p	p	f_p	ω_p	γ_p
1	1.1828	3.735	0.7	1	0.6383	3.1514	0.54
2	1.1502	0.9555	0.64	2	27.0133	0.3132	0.5

Figure 1 shows the spectral response of the refractive index, n and the extinction coefficient, k of VO₂ by using the parameters in Table 1. As the wavelength increases, k of VO₂ at high temperature increases gradually, however, that at low temperature is slightly changed.

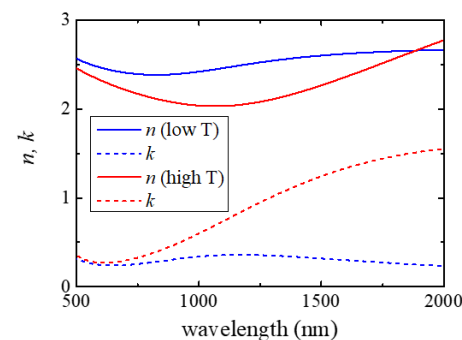


Figure 1. Dispersion of refractive index, n and extinction coefficient, k of the VO₂ thin film modelled by Drude–Lorentz equation, Equation (1).

2.2. Design of Geometrical Orientation of Au Nanorod

Based on PB-phase principle, a rotational angle of Au nanorod was determined. First, a desired phase was calculated. For horizontal beam steering, every single column of Au nanorod should make a constant phase change which was realized by rotating Au nanorod with half of the desired phase change. In case of Fourier hologram, a desired image was prepared with binary data, first. And then, the phase distribution was determined by two-dimensional fast Fourier transformation (2-D FFT) of the image with a random phase. Finally, the orientation of each Au nanorod was set as half of the calculated phase at a center position of Au nanorod. Design process of Au nanorods for Fresnel hologram was the same as Fourier hologram except the calculation of the phase distribution, which was calculated by Fresnel's pingpong algorithm [45].

2.3. Numerical Method

We investigated optical performances of reflectarray metasurfaces with VO₂ thin film by three-dimensional FDTD simulation [43]. For analyzing an amplitude and phase of a reflected light, the total-field/scattered-field method with the normal incident plane wave was used. Furthermore, a minimum spatial resolution was fixed at 4 nm for representing surface plasmon effect. In the beam steering and hologram simulation, the normal incident light was circularly polarized.

3. Applications and Discussions

3.1. Optimization of Reflectarray Metasurface with VO₂ Thin Film

VO₂ has the metal-insulator-transition behavior, and VO₂ based metasurface manipulating the polarization control has widely been demonstrated in the IR and THz region [37,41,46]. However, high-efficient VO₂ based metasurface in the visible range has not been reported yet. In this section, we proposed a simple metasurface with VO₂ thin film with Au nanorod array, which provides a great advantage for the fabrication. Figure 2a shows the schematic view of a reflectarray PB-phase metasurface. An array of Au nanorods is on top of a thin VO₂ film which lies on the Au thick film. The structural parameters of the Au nanorod are defined at Figure 2a. The optimized structural parameters of the Au nanorod (see Figure S1 in Supplementary Materials) are $w = 80$ nm and $L = 200$ nm when the period (a) and the thickness (t) is fixed at 300 nm and 30 nm, respectively. Here, the thickness of the VO₂ film is set as 80 nm which is close to the optimum value for polarization conversion (see Figure S3 in Supplementary Materials), and the thickness of the Au film is fixed at 150 nm. Figure 2b shows temperature dependent reflection spectra with different input polarization which direction corresponds to the l - or s -axis of the Au nanorod shown in the inset. At low temperature, the dips of R_l and R_s were found at 620 and 660 nm, respectively. According to Figure 2c, a phase difference, $\Delta\phi$ is around zero in the spectral region between two dips, however, $\Delta\phi$ is almost π in the longer wavelength. The same spectral response was observed at high temperature as the dips of R_l and R_s found at 690 nm and 730 nm, respectively. Especially, a spectrum subtracting two phase-difference spectra shown in Figure 2c is π near 700 nm. Hence, when temperature increases over the critical temperature, reflection at $\lambda \sim 700$ nm maintains over 65%, however, phase difference switches from π to zero. This implies that the structure could have a functionality of a metasurface only at low temperature.

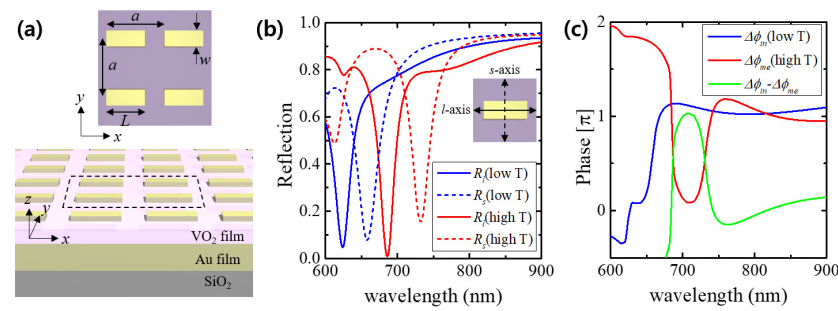


Figure 2. Reflectarray metasurface with VO₂ thin film (a) Schematics. (b) Temperature dependent reflection spectra with different polarization directions of the normal incident light. (c) Temperature dependent phase-difference spectra between *l*-axis and *s*-axis polarizations, and phase spectrum subtracting the two spectra.

3.2. Manipulation of Reflected Light

3.2.1. Polarization Conversion of Reflected Light

First, we numerically investigated polarization conversion efficiency by the optimized VO₂ based reflectarray metasurface structure consisted of a 45°-rotated Au nanorod. The details of the structure and characterization of 45°-rotated Au nanorod metasurface were described in Figure S2 at Supplementary Materials. Figure 3a,b show the polarization conversion ratio (*PCR*) at low temperature and that at the high temperature, respectively, defined as

$$PCR = \frac{R_{cr}}{R_{cr} + R_{co}}, \quad (2)$$

where R_{co} is the reflectance of the co-polarized light defined as $|E_{x,r}/E_{x,i}|^2$, and R_{cr} is the reflectance of the cross-polarized light defined as $|E_{y,r}/E_{x,i}|^2$. Here, E_i is the amplitude of the incident electric field and E_r is that of the reflected electric field. It is worth noting that if $PCR = 1$, all the reflected light is the cross-polarized light, and if $PCR = 0$, all the reflected light is the co-polarized light. As shown in Figure 3a, PCR is over 0.90 at low temperature in the NIR region (>750 nm). Furthermore, PCR is high at high temperature, but very low PCR (~ zero) is found near 700 nm. From these results, the proposed structure can act as a high efficient polarization conversion metasurface at all temperature in the NIR region. However, near 700 nm, polarization conversion occurs only at low temperature. As shown in Figure 3c, reflection spectra at $w = 80$ nm (the white lines marked in Figure 3a,b) clearly show this polarization conversion property. In the NIR region, R_{cr} is over 80%, while R_{co} is below 10% at both low and high temperature. However, at $\lambda \sim 700$ nm, R_{cr} is about 75% at low temperature, but almost zero (~0.5%) at high temperature.

3.2.2. Switchable Beam Steering

Second, switchable beam steering was investigated with the optimized VO₂ based reflectarray metasurface at $\lambda = 700$ nm by temperature change. The PB-phase metasurface is consisted of 12 Au nanorods by steps of 15° change from the left to the right (see the right inset of Figure 3d). In the calculation, the input beam with the left-handed circular polarization (LCP) or the right-handed circular polarization (RCP) was used, and the polarization state of the reflected beam was analyzed by the angular radiation pattern from near-to-far-field transformation algorithm [47]. Figure 3d shows the polarization dependent angular radiation patterns of the reflected light. When the input polarization was LCP at low temperature, the reflected light was RCP with radiation angle, $\sim 11^\circ$ along the horizontal direction, which is well matched with the designed radiation angle defined as $\tan^{-1}(12a/\lambda)$. However, at high temperature, the reflected light had the same polarization in the normal direction. In case of the RCP input beam, the beam steering behavior was only observed at low temperature, too. Hence, switchable beam steering was successfully demonstrated at $\lambda = 700$ nm by temperature change.

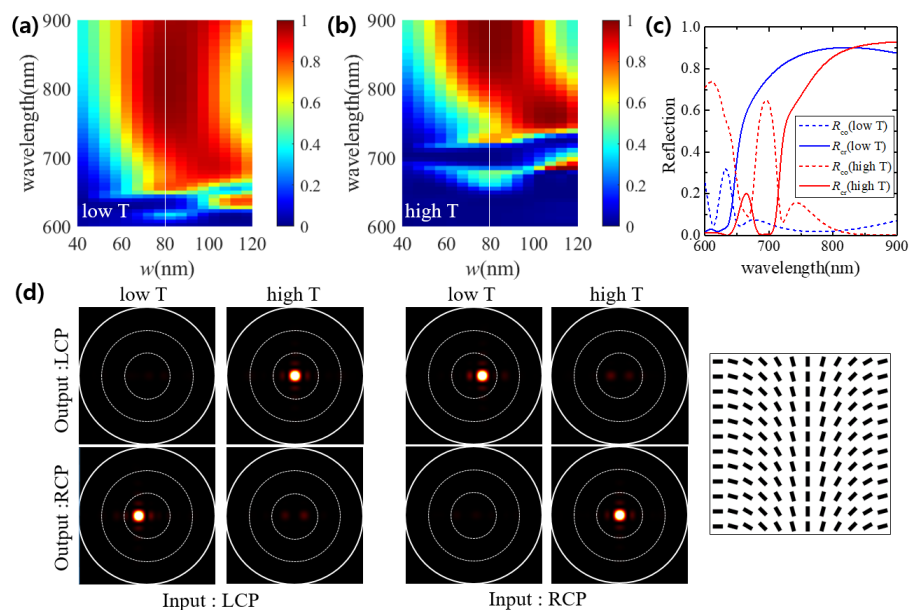


Figure 3. Characteristics of metasurface. (a) Thickness-dependent reflection spectral map at low temperature and (b) at high temperature. (c) Reflection spectra of the co-polarized and cross-polarized light at low temperature and high temperature marked with white lines in (a,b). (d) Manipulation of beam steering with different input polarization at $\lambda = 700$ nm. Inset in the right is the in-plane cut view of Au nanorods in the metasurface.

3.2.3. Beam Steering with Continuous Phase Change of VO₂ Film

We numerically investigated PCR of the optimized reflectarray metasurface with various degree of metallic phase of VO₂ film. The Drude–Lorentz parameters for dielectric constant of VO₂ with partial metallic phase were estimated by Bruggeman effective medium theory (see Supplementary Materials) [35,48]. As shown in Figure 4a, reflection spectra is red-shift as a volume fraction of metallic phase of VO₂, f increases because of decreasing n . Consequently, PCR spectra is also red-shift (see Figure 4b). Especially, PCR is maintained over 70% at $\lambda = 700$ nm when f increases until 0.5. However, PCR suddenly decreases with further increasing f , and finally becomes zero at metal phase ($f = 1$). In consideration of complete phase change within small temperature difference, PCR is very sensitive to temperature near the critical temperature [35]. In order to confirm sensitivity of PCR to temperature, we investigated beam steering as a function of degree of metal phase in VO₂ film. According to Figure 4d, as f increases, the cross-polarized light reflected at radiation angle, $\sim 11^\circ$ becomes weak. In contrast, the co-polarized light in normal reflection becomes strong which is well matched with Figure 4c. This result implies that radiation direction could be switched continuously without change of radiation angle by continuous phase change of VO₂ film.

3.3. Fourier Hologram

One of famous applications with metasurfaces is a hologram. According to the distance from a hologram to a reconstructed image, types of holograms can be classified [49]. The image hologram is a hologram to record a real image of the object formed by a lens. So the reconstructed image lies on the hologram. The Fresnel hologram is a hologram to record the near-field diffraction pattern of the object. Therefore, the reconstructed image is located near the hologram. The Fourier hologram is a hologram to record an interference pattern between Fourier transforms of the object and a collimated beam. So the object is placed in the front focal plane of a lens and the hologram is in the back focal plane of the lens. The reconstructed image is located in the far field, so to visualize the image, it is necessary to use another lens to form the image. We demonstrated switchable metasurface Fourier hologram at $\lambda = 700$ nm which was designed by a computer generated hologram (CGH)

technique [50]. Figure 5 shows the performance of Fourier hologram generated by the optimized VO₂-film based reflectarray metasurface. The letter images at the left column in Figure 5 were prepared with 32 × 32-pixel binary images. Two middle columns in Figure 5 indicate the phase maps calculated by 2-D FFT and corresponding Au nanorod arrays, respectively. At low temperature, the holographic images were reconstructed as shown in the second right column. The speckle pattern on the holographic image is due to the random phase. At high temperature, the normal reflected lights were observed as shown in the right column, which correspond to the zeroth order diffraction. From this, we expect that the far-field image generated by VO₂ based reflectarray metasurface Fourier hologram can be switchable by temperature.

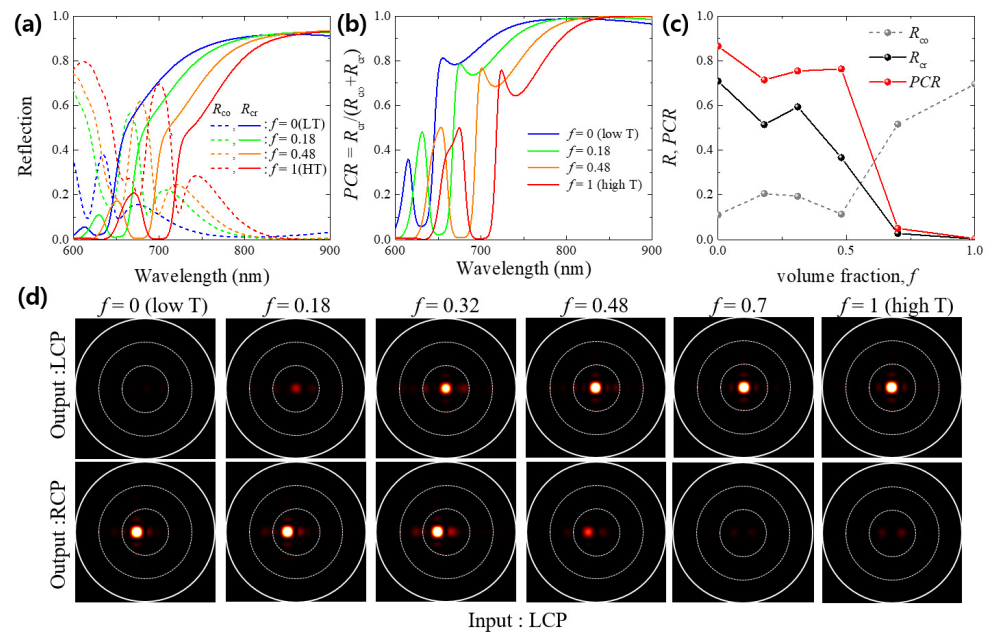


Figure 4. Characteristics of reflectivity in reflectarray metasurface with VO₂ thin film at different volume fraction of metal phase. (a) Reflection spectra of the co-polarized and cross-polarized light (b) PCR spectra (c) Reflection and PCR at $\lambda = 700$ nm. (d) Manipulation of beam steering.

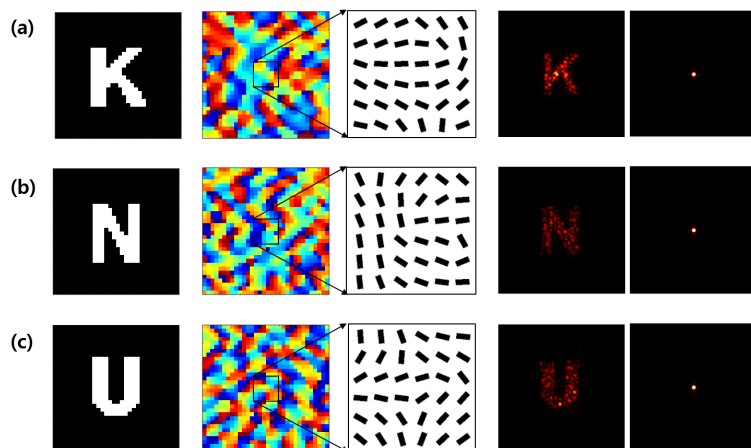


Figure 5. Switchable Fourier hologram generated by VO₂ based reflectarray metasurface with the character (a) K (b) N, and (c) U. The columns from the left to the right indicate the original binary image, phase map, magnified in-plane cut-view of Au nanorod array, and reconstructed far-field images with $\lambda = 700$ nm projected in the polar coordinate at low temperature and high temperature.

3.4. Fresnel Hologram

To investigate optical switching of the near-field hologram image in the visible region, we demonstrated the Fresnel hologram with the optimized VO₂ based reflectarray metasurface at $\lambda = 700$ nm. First, we prepared a 32×32 -pixel binary image of a smiling face (Figure 6a) and calculated the phase distribution (Figure 6b) by CGH technique based on Fresnel' pingpong algorithm [45]. According to the phase distribution, the optimal Au nanorods were arranged based on PB-phase principle (Figure 6c). Here, we designed a reflectarray metasurface hologram with an image plane at $10 \mu\text{m}$ from the metasurface. Figure 6d shows the time-averaged intensity distribution at the image plane at low temperature, which agrees well with the original smiling face. However, at high temperature, the reconstructed image appears weakly because R_{co} component contributes to generate the smile image. Therefore, if the polarizer to remove the co-polarization component or off-axis hologram technique is adapted, switchable hologram on temperature could be realized. For the quantitative analysis, we calculated the signal-to-noise ratio (SNR) of the time-averaged intensity. In case of low temperature, $\text{SNR} \sim 16.5$ dB, however, $\text{SNR} \sim 8.2$ dB at high temperature. The SNR could be enhanced if the area of metasurface hologram increases. We also obtained the depth-of-field (DOF) in the holographic image at low temperature. According to the time-averaged intensity distributions obtained from different z -position shown in Figure 6f, DOF is estimated about $4\lambda \simeq 3 \mu\text{m}$.

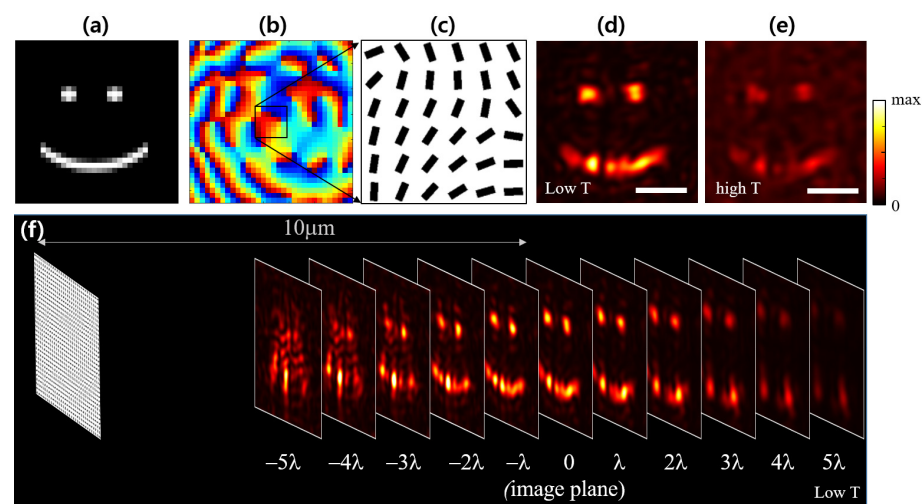


Figure 6. Switchable Fresnel hologram performed by VO₂ based reflectarray metasurface at $\lambda = 700$ nm. (a) Original smile image (b) Phase map (c) In-plane cut-view of Au nanorod array (d) Time-averaged intensity distribution at the image plane at low temperature, and (e) at high temperature. (f) Evolution of the time-averaged intensity distribution with a distance from the image plane ($z = 10 \mu\text{m}$). The white scale bars in (d,e) indicate $3 \mu\text{m}$.

4. Conclusions

We numerically demonstrated switchable metasurfaces using a thin-VO₂-film based reflectarray of Au nanorods in the visible region at $\lambda = 700$ nm. First, the optical constants of VO₂ from insulating phase at low temperature to metallic phase at high temperature was modelled by the Drude–Lorentz equation with Bruggeman effective medium theory in the visible to the IR region. An Au nanorod on top of a thin VO₂ film above a thick Au film was optimized for high polarization conversion efficiency only at low temperature. The optimized reflectarray metasurface shows polarization conversion efficiency about 75% at $\lambda = 700$ nm at low temperature, while the polarization conversion efficiency is less than 0.5% at high temperature. We numerically demonstrated various performances of switchable metasurfaces, such as polarization conversion, beam steering, Fourier hologram, and Fresnel hologram. The PB-phase principle was adapted to realize an arbitral phase distribution by controlling the angle of Au nanorods. We believe that the thin-VO₂-film-

based switchable metasurface in the visible region can be a practical platform for various applications of dynamic optical switch devices by temperature, such as optical sensors, beam forming antennas, and display.

Supplementary Materials: The following are available online at <https://www.mdpi.com/2304-6732/8/2/57/s1>, Figure S1: Optimization of the Au nanorod in a VO₂ based reflectarray metasurface, Figure S2: Characterization of a VO₂ based reflectarray metasurface consisting of the 45°-rotated Au nanorods, Figure S3: Reflection spectra with different thickness of VO₂ film, Figure S4: Dispersions of dielectric constant (ϵ) with various volume fractions (f) of metallic phases of VO₂, Table S1: The values of volume fraction f and depolarization factor q at different temperature and the parameters of two poles of the Drude–Lorentz model for dielectric constant of VO₂.

Author Contributions: Conceptualization, J.-K.Y.; methodology, J.-K.Y. and H.-S.J.; investigation, J.-K.Y. and H.-S.J.; data curation, J.-K.Y.; writing—original draft preparation, J.-K.Y.; writing—review and editing, J.-K.Y. All authors have read and agreed to the published version of the manuscript.

Funding: This work was supported by the research grant of the Kongju National University in 2019.

Institutional Review Board Statement: Not applicable.

Informed Consent Statement: Not applicable.

Data Availability Statement: Data available on request due to restrictions eg privacy or ethical. The data presented in this study are available on request from the corresponding author.

Acknowledgments: The authors thank H.-S. Ee for fruitful discussion for numerical calculations.

Conflicts of Interest: The authors declare no conflict of interest.

References

1. Yu, N.; Genevet, P.; Kats, M.A.; Aieta, F.; Tetienne, J.P.; Capasso, F.; Gaburro, Z. Light Propagation with Phase Discontinuities: Generalized Laws of Reflection and Refraction. *Science* **2011**, *334*, 333–337. [[CrossRef](#)]
2. Yu, N.; Capasso, F. Flat optics with Designer Metasurfaces. *Nat. Mater.* **2014**, *13*, 139–150. [[CrossRef](#)] [[PubMed](#)]
3. Staude, I.; Schilling, J. Metamaterial-Inspired Silicon Nanophotonics. *Nat. Photonics* **2017**, *11*, 274–284. [[CrossRef](#)]
4. Huang, L.; Chen, X.; Mühlenbernd, H.; Li, G.; Bai, B.; Tan, Q.; Jin, G.; Zentgraf, T.; Zhang, S. Dispersionless Phase Discontinuities for Controlling Light Propagation. *Nano Lett.* **2012**, *12*, 5750–5755. [[CrossRef](#)] [[PubMed](#)]
5. Ma, X.; Pu, M.; Li, X.; Huang, C.; Wang, Y.; Pan, W.; Zhao, B.; Cui, J.; Wang, C.; Zhao, Z.; et al. A Planar Chiral Meta-Surface for Optical Vortex Generation and Focusing. *Sci. Rep.* **2015**, *5*, 10365. [[CrossRef](#)]
6. Mehmood, M.Q.; Mei, S.; Hussain, S.; Huang, K.; Siew, S.Y.; Zhang, L.; Zhang, T.; Ling, X.; Liu, H.; Teng, J. Visible-Frequency Metasurface for Structuring and Spatially Multiplexing Optical Vortices. *Adv. Mater.* **2016**, *28*, 2533–2539. [[CrossRef](#)]
7. Yue, F.; Wen, D.; Xin, J.; Gerardot, B.D.; Li, J.; Chen, X. Vector Vortex Beam Generation with a Single Plasmonic Metasurface. *ACS Photonics* **2016**, *3*, 1558–1563. [[CrossRef](#)]
8. Yu, N.; Aieta, F.; Genevet, P.; Kats, M.A.; Gaburro, Z.; Capasso, F. A Broadband, Background-Free Quarter-Wave Plate Based on Plasmonic Metasurfaces. *Nano Lett.* **2012**, *12*, 6328–6333. [[CrossRef](#)]
9. Jiang, Z.H.; Lin, L.; Ma, D.; Yun, S.; Werner, D.H.; Liu, Z.; Mayer, T.S. Broadband and Wide Field-of-View Plasmonic Metasurface-Enabled Waveplates. *Sci. Rep.* **2014**, *4*, 7511. [[CrossRef](#)]
10. Ding, F.; Wang, Z.; He, S.; Shalaev, V.M.; Kildishev, A.V. Broadband high-efficiency half-wave plate: A Supercell-Based Plasmonic Metasurface Approach. *ACS Nano* **2015**, *9*, 4111–4119. [[CrossRef](#)]
11. Kim, J.; Choudhury, S.; DeVault, C.; Zhao, Y.; Kildishev, A.V.; Shalaev, V.M.; Alù, A.; Boltasseva, A. Controlling the Polarization State of Light with Plasmonic Metal Oxide Metasurface. *ACS Nano* **2016**, *10*, 9326–9333. [[CrossRef](#)]
12. Ren, M.-X.; Wu, W.; Cai, W.; Pi, B.; Zhang, X.-Z.; Xu, J.-J. Reconfigurable Metasurfaces That Enable Light Polarization Control by Light. *Light Sci. Appl.* **2017**, *6*, e16254. [[CrossRef](#)] [[PubMed](#)]
13. Aieta, F.; Genevet, P.; Kats, M.A.; Yu, N.; Blanchard, R.; Gaburro, Z.; Capasso, F. Aberration-Free Ultrathin Flat Lenses and Axicons at Telecom Wavelengths Based on Plasmonic Metasurfaces. *Nano Lett.* **2012**, *12*, 4932–4936. [[CrossRef](#)] [[PubMed](#)]
14. Khorasaninejad, M.; Chen, W.T.; Devlin, R.C.; Oh, J.; Zhu, A.Y.; Capasso, F. Metalenses at Visible Wavelengths: Diffraction-Limited Focusing and Subwavelength Resolution Imaging. *Science* **2016**, *352*, 1190–1194. [[CrossRef](#)]
15. Arbabi, A.; Arbabi, E.; Kamali, S.M.; Horie, Y.; Han, S.; Faraon, A. Miniature Optical Planar Camera Based on a Wide-Angle Metasurface Doublet Corrected for Monochromatic Aberrations. *Nat. Commun.* **2016**, *7*, 13682. [[CrossRef](#)] [[PubMed](#)]
16. Chen, W.T.; Zhu, A.Y.; Capasso, F. Flat Optics with Dispersion-Engineered Metasurfaces. *Nat. Rev. Mater.* **2020**, *5*, 604. [[CrossRef](#)]
17. Ni, X.; Kildishev, A.V.; Shalaev, A.V.M. Metasurface Holograms for Visible Light. *Nat. Commun.* **2013**, *4*, 2807. [[CrossRef](#)]
18. Zheng, G.; Mühlenbernd, H.; Kenney, M.; Li, G.; Zentgraf, T.; Zhang, S. Metasurface Holograms Reaching 80% Efficiency. *Nat. Nanotechnol.* **2015**, *10*, 308–312. [[CrossRef](#)]

19. Wen, D.; Yue, F.; Li, G.; Zheng, G.; Chan, K.; Chen, S.; Chen, M.; Li, K.F.; Wong, P.W.H.; Cheah, K.W.; et al. Helicity Multiplexed Broadband Metasurface Holograms. *Nat. Commun.* **2015**, *6*, 8241. [[CrossRef](#)]
20. Arbabi, A.; Horie, Y.; Ball, A.; Bagheri, M.; Faraon, A. Subwavelength-Thick Lenses with High Numerical Apertures and Large Efficiency Based on High-Contrast Transmitarrays. *Nat. Commun.* **2015**, *6*, 7069. [[CrossRef](#)] [[PubMed](#)]
21. Ren, H.; Fang, X.; Jang, J.; Bürger, J.; Rho, J.; Maier, S.A. Complex-Amplitude Metasurface-Based Orbital Angular Momentum Holography in Momentum Space. *Nat. Nanotechnol.* **2020**, *15*, 948–955. [[CrossRef](#)] [[PubMed](#)]
22. Sun, S.; Yang, K.-Y.; Wang, C.-M.; Juan, T.-K.; Chen, W.T.; Liao, C.Y.; He, Q.; Xiao, S.; Kung, W.-T.; Guo, G.-Y. High-Efficiency Broadband Anomalous Reflection by Gradient Meta-Surfaces. *Nano Lett.* **2012**, *12*, 6223–6229. [[CrossRef](#)]
23. Ni, X.; Emani, N.K.; Kildishev, A.V.; Boltasseva, A.; Shalaev, V.M. Broadband Light Bending with Plasmonic Nanoantennas. *Science* **2012**, *335*, 427. [[CrossRef](#)] [[PubMed](#)]
24. Kang, M.; Feng, T.; Wang, H.T.; Li, J. Wave Front Engineering from an Array of Thin Aperture Antennas. *Opt. Express* **2012**, *20*, 15882–15890. [[CrossRef](#)]
25. Lin, D.; Fan, P.; Hasman, E.; Brongersma, M.L. Dielectric Gradient Metasurface Optical Elements. *Science* **2014**, *345*, 298–302. [[CrossRef](#)]
26. Khorasaninejad, M.; Crozier, K.B. Silicon Nanofin Grating as a Miniature Chirality-Distinguishing Beam-Splitter. *Nat. Commun.* **2014**, *5*, 5386. [[CrossRef](#)]
27. Staude, I.; Miroshnichenko, A.E.; Decker, M.; Fofang, N.T.; Liu, S.; Gonzales, E.; Dominguez, J.; Luk, T.S.; Neshev, D.N.; Brener, I.; et al. Tailoring Directional Scattering through Magnetic and Electric Resonances in Subwavelength Silicon Nanodisks. *ACS Nano* **2013**, *7*, 7824–7832. [[CrossRef](#)]
28. Decker, M.; Staude, I.; Falkner, M.; Dominguez, J.; Neshev, D.N.; Brener, I.; Pertsch, T.; Kivshar, Y.S. High-Efficiency Dielectric Huygens' Surfaces. *Adv. Opt. Mater.* **2015**, *3*, 813–820. [[CrossRef](#)]
29. Iyer, P.P.; Butakov, N.A.; Schuller, J.A. Reconfigurable Semiconductor Phased-Array Metasurfaces. *ACS Photonics* **2015**, *2*, 1077. [[CrossRef](#)]
30. Ee, H.S.; Agarwal, R. Tunable Metasurface and Flat Optical Zoom Lens on a Stretchable Substrate. *Nano Lett.* **2016**, *16*, 2818–2823. [[CrossRef](#)] [[PubMed](#)]
31. Huang, Y.-W.; Lee, H.W.H.; Sokhoyan, R.; Pala, R.A.; Thyagarajan, K.; Han, S.; Tsai, D.P.; Atwater, H.A. Gate-Tunable Conducting Oxide Metasurfaces. *Nano Lett.* **2016**, *16*, 5319–5325. [[CrossRef](#)]
32. Wang, Q.; Rogers, E.T.F.; Gholipour, B.; Wang, C.-M.; Yuan, G.; Teng, J.; Zheludev, N.I. Optically Reconfigurable Metasurfaces and Photonic Devices Based on Phase Change Materials. *Nat. Photonics* **2016**, *10*, 60–65. [[CrossRef](#)]
33. Shaltout, A.M.; Shalaev, V.M.; Brongersma, M.L. Spatiotemporal Light Control with Active Metasurfaces. *Science* **2019**, *364*, eaat3100. [[CrossRef](#)]
34. Hosseini, P.; Wright, C.D.; Bhaskaran, H. An Optoelectronic Framework Enabled by Low-Dimensional Phase-Change Films. *Nature* **2014**, *511*, 206–211. [[CrossRef](#)]
35. Qazilbash, M.M.; Brehm, M.; Andreev, G.O.; Kim, B.J.; Yun, S.J.; Balatsky, A.V.; Maple, M.B.; Keilmann, F.; Kim, H.T.; Basov, D.N. Mott Transition in VO₂ Revealed by Infrared Spectroscopy and Nano-Imaging. *Science* **2007**, *318*, 1750–1753. [[CrossRef](#)]
36. Kats, M.A.; Sharma, D.; Lin, J.; Genevet, P.; Blanchard, R.; Yang, Z.; Qazilbash, M.M.; Basov, D.N.; Ramanathan, S.; Capasso, F. Ultra-Thin Perfect Absorber Employing a Tunable Phase Change Material. *Appl. Phys. Lett.* **2012**, *101*, 221101. [[CrossRef](#)]
37. Shao, Z.; Cao, X.; Luo, H.; Jin, P. Recent Progress in the Phase-Transition Mechanism and Modulation of Vanadium Dioxide Materials. *NPG Asia Mater.* **2018**, *10*, 581–605. [[CrossRef](#)]
38. Kang, L.; Jenkins, R.P.; Werner, D.H. Recent Progress in Active Optical Metasurfaces. *Adv. Opt. Mater.* **2019**, *7*, 1801813. [[CrossRef](#)]
39. He, Q.; Sun, S.; Zhou, L. Tunable/Reconfigurable Metasurfaces: Physics and Applications. *Research* **2019**, *2019*, 1849272. [[CrossRef](#)]
40. Duan, X.; White, S.T.; Cui, Y.; Neubrech, F.; Gao, Y.; Haglund, R.F.; Liu, N. Reconfigurable Multistate Optical Systems Enabled by VO₂ Phase Transitions. *ACS Photonics* **2020**, *7*, 2958–2965. [[CrossRef](#)]
41. Chen, W.; Chen, R.; Zhou, Y.; Chen, R.; Ma, Y. Spin-dependent switchable metasurfaces using phase change materials. *Opt. Express* **2019**, *27*, 25678–25687. [[CrossRef](#)]
42. Kana, J.B.K.; Ndjaka, J.M.; Vignaud, G.; Gibaud, A.; Maaza, M. Thermally Tunable Optical Constants of Vanadium Dioxide Thin Films Measured by Spectroscopic Ellipsometry. *Opt. Commun.* **2011**, *284*, 807–812. [[CrossRef](#)]
43. Ee, H.S.; Song, K.D.; Kim, S.K.; Park, H.G. Finite-Difference Time-Domain Algorithm for Quantifying Light Absorption in Silicon Nanowires. *Isr. J. Chem.* **2012**, *52*, 1027–1036. [[CrossRef](#)]
44. Currie, M.; Mastro, M.A.; Wheeler, V.D. Characterizing the Tunable Refractive Index of Vanadium Dioxide. *Opt. Mater. Express* **2017**, *7*, 1697–1707. [[CrossRef](#)]
45. Malek, S.C.; Ee, H.S.; Agarwal, R. Strain multiplexed metasurface holograms on a stretchable substrate. *Nano Lett.* **2017**, *6*, 3641–3645. [[CrossRef](#)]
46. Ding, F.; Zhong, S.; Bozhevolnyi, S.I. Vanadium Dioxide Integrated Metasurfaces with Switchable Functionalities at Terahertz Frequencies. *Adv. Opt. Mater.* **2018**, *6*, 1701204. [[CrossRef](#)]
47. Demarest, K.; Huang, Z.; Plumb, R. An FDTD Near-to Far-zone Transformation for Scatterers Buried in Stratified Grounds. *IEEE Trans. Antennas Propag.* **1996**, *44*, 1150–1157. [[CrossRef](#)]
48. Kim, Y.; Wu, P.C.; Sokhoyan, R.; Mauser, K.; Glaudell, R.; Kafaie Shirmanesh, G.; Atwater, H.A. Phase modulation with electrically tunable vanadium dioxide phase-change metasurfaces. *Nano Lett.* **2019**, *19*, 3961–3968. [[CrossRef](#)]

-
49. Jiang, Q.; Jin, G.; Cao, L. When Metasurface Meets Hologram: Principle and Advances. *Adv. Opt. Photonics* **2019**, *11*, 518–576. [[CrossRef](#)]
 50. Wyrowski, F.; Bryngdahl, O. Iterative Fourier-Transform Algorithm Applied to Computer Holography. *J. Opt. Soc. Am. A* **1988**, *5*, 1058–1065. [[CrossRef](#)]